RSC Advances

PAPER

View Article Online
View Journal | View Issue

Cite this: *RSC Adv.*, 2025, **15**, 10037

Design, nanogel synthesis, anti-proliferative activity and *in silico* ADMET profile of pyrazoles and pyrimidines as topo-II inhibitors and DNA intercalators†

Ahmed K. B. Aljohani,[a] Sanadelaslam S. A. El-Hddad,[b] Marwa Alsulaimany,[a] Nader A. Maghrabi,[c] Alaa M. Alhammad,[c] Mayar N. Aloufi,[c] Luai F. Alahmadi,[c] Turkiah Ali Saeedi,[c] Yousef Yakoub Neyaz,[c] Kurls E. Anwer,[d] Nour E. A. Abd El-Sattar[de] and Khaled El-Adl[*fg]

Pyrazole derivatives **2** and **3**, pyrimidine derivative **4**, and their nanogels as drug delivery systems were synthesized, and their cytotoxicity against MCF-7, HCT-116, HepG2 and A549 cells was evaluated. Herein, we focused on the characterization and synthesis of chitosan/polyvinyl alcohol (Cs/PVA) nanogels loaded with derivatives **2**, **3** and **4**. The stability of the prepared nanogels **2**, **3** and **4** was elucidated by zeta potential measurements, which possessed negative values of −9.7, −1.3 and −1.6 mV, respectively. Our compounds and their nanogels were evaluated as topo-II inhibitors and DNA intercalators. The nanogel delivery system enhanced the cytotoxicity of compound **2** against the A549, HCT116, HepG2 and MCF-7 cancer cell lines by 32.06%, 28.96%, 44.32% and 50.00%, respectively. Moreover, the nanogel of compound **3** exhibited enhanced cytotoxicity against the A549, HCT116, HepG2 and MCF-7 cancer cell lines by 33.61%, 30.64%, 44.69% and 47.86%, respectively. Furthermore, the nanogel of compound **4** showed enhanced cytotoxicity against the A549, HCT116, HepG2 and MCF-7 cancer cell lines by 31.82%, 40.12%, 50.00% and 52.61%, respectively. Moreover, derivatives **2**, **2 (nanogel)**, **3**, **3 (nanogel)**, **4** and **4 (nanogel)** exhibited good selectivity against cancer cells and reduced toxicity to VERO cells with IC_{50} values in the range of 48.29–59.70 μM. Furthermore, our derivatives displayed remarkable *in silico* predicted ADMET profiles.

Received 7th January 2025
Accepted 17th March 2025

DOI: 10.1039/d5ra00166h

rsc.li/rsc-advances

1. Introduction

Small organic compounds can bind non-covalently to nucleic acids with prospective anticancer activities.[1] Their binding can interrupt transcription and/or replication, leading to cellular death. These molecules can intercalate into DNA, inserting themselves between its base pairs, and interact through electrostatic forces, binding to the minor or major grooves.[2] DNA intercalator agents should possess the following crucial structural features: (i) groove binding side chain,[3,4] (ii) basic amino groups[5] and (iii) planar polyaromatic chromophores.[6–8]

The two types of intercalator agents are classic and threading intercalators.[9] Threading intercalators have two groove binding side chains oriented to the major and minor grooves.[10]

Currently, several DNA intercalators are used as anticancer agents or are under clinical trials (*e.g.*, amsacrine **I**,[11] doxorubicin **II**,[12] ellipticine **III**,[13] and EBE-A22 **IV**[14]) (Fig. 1).

Pyrazole derivatives have shown diverse pharmacological and biological effects. As potential anticancer agents, they have shown strong anti-proliferative activity on tumor cells, multiple targets and good selectivity *in vitro*. To date, many pyrazole derivatives have been reported as DNA intercalators and topoisomerase II enzyme inhibitors.[15]

Moreover, many pyrimidine derivatives have been reported as topo-II inhibitors and DNA intercalators. Merbarone (**V**) prevents DNA cleavage by inhibiting topo-II and blocking the catalytic cycle after DNA cleavage but before DNA degradation.[16]

[a]*Department of Pharmacognosy & Pharmaceutical Chemistry, College of Pharmacy, Taibah University, Medina, 42353, Saudi Arabia*
[b]*Pharmaceutical Chemistry Department, Faculty of Pharmacy, Omar Almukhtar University, Al Bayda 991, Libya*
[c]*Pharmacy Student, College of Pharmacy, Taibah University, Medina, Saudi Arabia*
[d]*Department of Chemistry, Faculty of Science, Ain Shams University, Abbassia, Cairo, Egypt*
[e]*Basic & Medical Sciences Department, Faculty of Dentistry, Alryada University for Science & Technology, Egypt*
[f]*Chemistry Department, Faculty of Pharmacy, Heliopolis University for Sustainable Development, Cairo, Egypt. E-mail: eladlkhaled74@yahoo.com; khaled.eladl@hu.edu.eg*
[g]*Pharmaceutical Medicinal Chemistry and Drug Design Department, Faculty of Pharmacy (Boys), Al-Azhar University, Nasr City 11884, Cairo, Egypt. E-mail: eladlkhaled74@azhar.edu.eg*

† Electronic supplementary information (ESI) available. See DOI: https://doi.org/10.1039/d5ra00166h

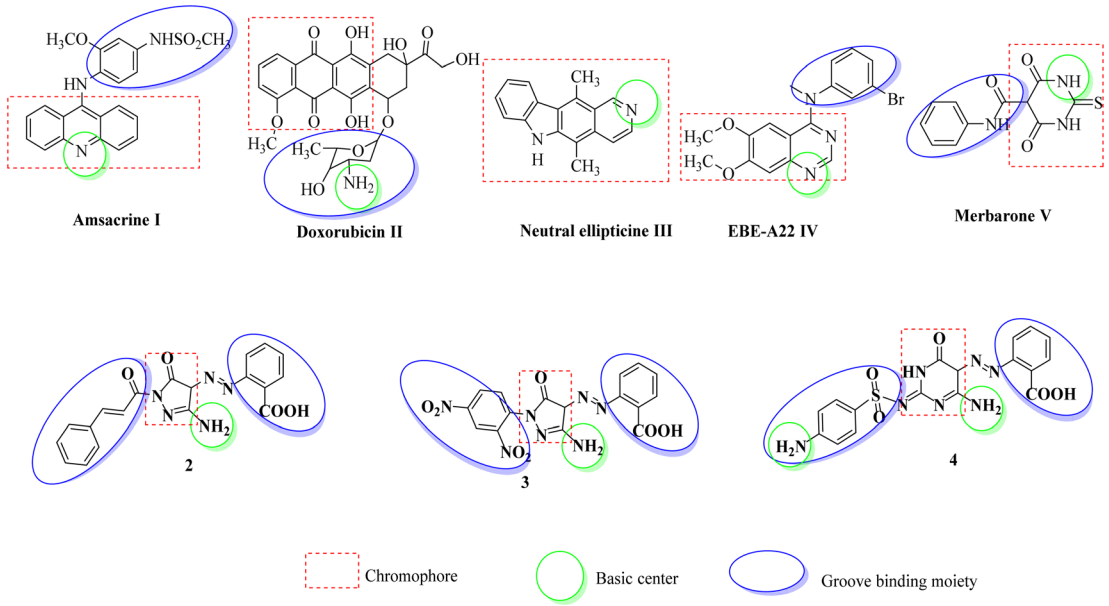

Fig. 1 Basic pharmacophoric features and rationale of our new DNA-intercalators.

Presently, nanocarriers are being developed with the aim of enhancing the efficacy of medications and reducing the dangerous side effects. These carriers are intended to release drugs in a well-ordered mode continuously and directly to cancer cells, leading to an enhanced uptake by cancer cells and improved drug targeting. Nanoparticles can be mechanically programmed to recognize cancer cells and selectively deliver drugs, evading healthy cells. Furthermore, nanocarriers as drug delivery systems have effectively overcome numerous restrictions, for example chemotherapy resistance, decreased solubility, toxicity, narrow therapeutic windows and poor oral absorption. These developments have paved the way for further effective cancer remedies.[17]

In addition, nanotechnology has been extended to the field of biomedicine, proposing widespread applications. Targeting nanoparticles are usually employed in numerous cancer studies owing to their capability to improve the bioavailability and reduce the side effects of drugs and display favorable anticancer properties compared to drugs administered in their free form.[18] In the field of nanomedicine, numerous nanocarriers have been employed due to their unique properties, such as the ability to transfer medicinally active ingredients to targeted locations because of their nanoscale proportions and high surface-to-volume proportion.[19] Furthermore, advanced pharmaceutical nanocarriers establish diverse valuable properties, such as improved intracellular permeation with the help of surface-attached cell-penetrating molecules; targeting at certain disease sites due to attached ligands on the surface of nanocarriers; accumulation in pathological areas with compromised vasculature; stability in the blood; loading of carriers with various contrast materials, leading to contrast properties, and consequently permitting the direct *in vivo* visualization of the carrier; and drug release from the carriers achieved by stimuli-sensitivity under specific physiological conditions. Some of these pharmaceutical carriers are still under preclinical development, while others have now made their way into clinic.[20,21]

Based on previous results, and in continuance of our preceding investigations on anticancer agents,[22–34] particularly DNA intercalators,[35–38] herein, we reported the DNA binding of novel anticancer pyrazoles and pyrimidines.

1.1. Rationale and structure-based design

Our rationale is based on planer pyrazole and/or pyrimidine rings (chromophore) with two side chains as groove binders. The synthesis was started by cyclization reactions to obtain pyrazole and/or pyrimidine nucleuses possessing a 2-diazenylbenzoic acid side chain and another different side chain (Fig. 1) as potential topo-II inhibitors and threading DNA intercalators.

All the structures were created to possess the main pharmacophoric properties of DNA intercalators, where the chromophore was exemplified by pyrazole and/or pyrimidine nucleuses intercalating DNA base pairs. In addition, all the derivatives have basic amino groups that may form cationic centers after protonation at physiological pH. Additionally, all the derivatives have two side chains oriented to the minor and the major grooves, increasing their DNA binding affinities.

Generally, the obtained derivatives were evaluated for their anti-proliferative cytotoxicity on HepG2, A549, MCF-7, and HCT-116 cells. The outcomes encouraged us to perform additional investigations regarding their mode of action.

Additionally, our derivatives were investigated for binding with DNA and inhibition of topo-II assays.

2. Results and discussion

2.1. Chemistry

The reaction of anthranilic acid with $NaNO_2$ in the presence of HCl at 0–5 °C produced the corresponding diazonium chloride

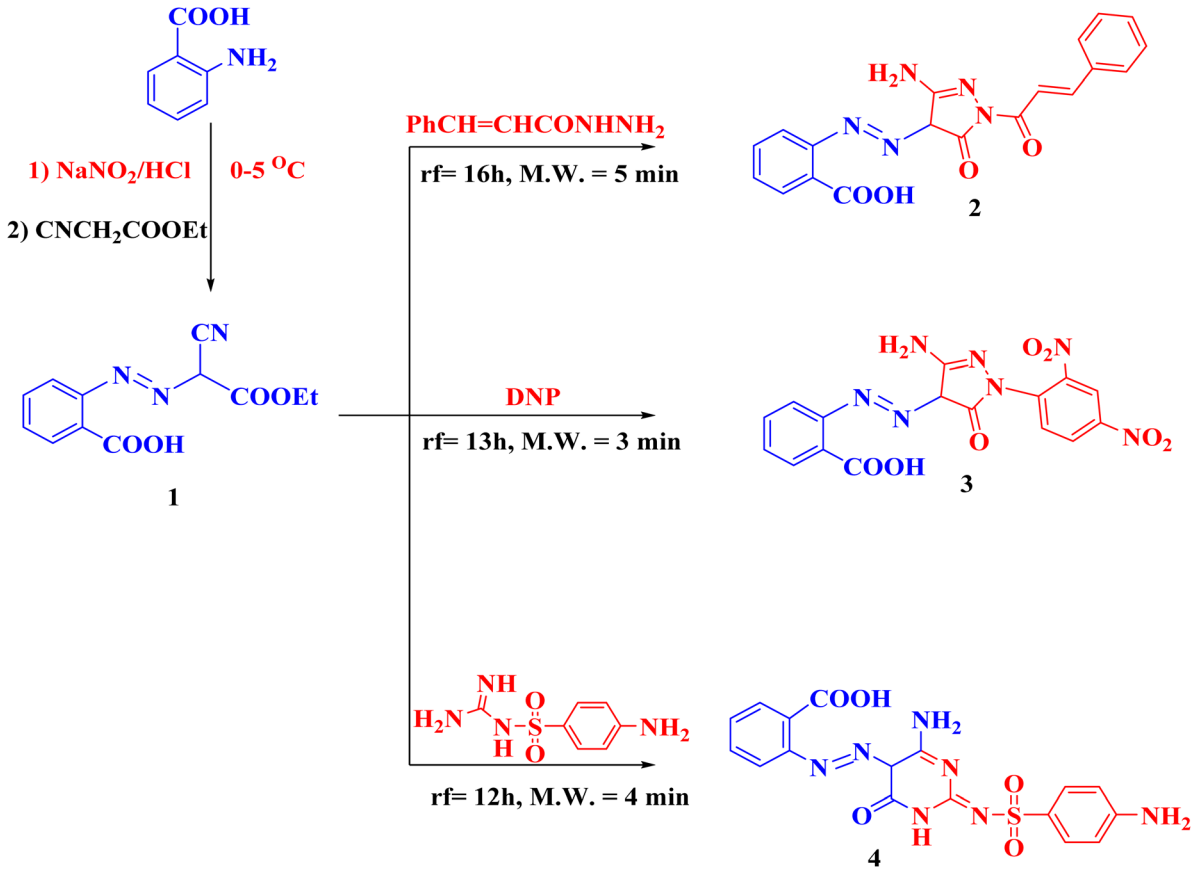

Scheme 1 Synthesis of the derivatives 1–4.

salt, which was coupled with ethyl cyanoacetate to yield the starting compound 2-((1-cyano-2-ethoxy-2-oxoethyl)diazenyl) benzoic acid **1** following the reported procedure.[39,40] Compound **1** was cyclized with the appropriate cinnamohydrazide and/or 2,4-dinitrophenyl hydrazine (DNP) to give the targeted pyrazolones **2** and **3**, respectively. Derivative **1** was used to synthesize the novel pyrimidine derivative **4** through cyclization reactions with sulphaguanidine (Scheme 1).

2.2. Nanogel preparation

2.2.1. UV-vis spectroscopic analysis of drug-loaded Cs/PVA nanogels. The UV-vis spectroscopic analysis presented in Fig. 2 provides compelling evidence for the successful incorporation of compounds **2**, **3**, and **4** into the Cs/PVA nanogel matrix. The spectral data revealed distinct absorption patterns, confirming the presence and integration of each drug within the nanogel structure. The pure Cs/PVA nanogel exhibited minimal absorption in the UV-visible region, serving as a clear baseline for comparison with the drug-loaded systems. The compound **2**-loaded nanogel demonstrated characteristic absorption peaks at specific wavelengths, with a notable increase in absorption intensity compared to the pure nanogel. This enhancement in absorption corresponds to the aromatic chromophores present in the structure of compound **2**, confirming its successful incorporation in the nanogel matrix. The observed bathochromic shift in the absorption maximum of the drug compared to its free form suggests strong interactions between compound **3** and the polymer matrix, likely through hydrogen bonding between the functional groups in the drug and the hydroxyl groups of PVA and amino groups of chitosan.

The spectral profile of the compound **2**-loaded nanogel shows distinct absorption bands that differ from that of both the pure nanogel and compound **2**-loaded system. The presence of well-defined peaks indicates the stable incorporation of the drug within the nanogel network. The observed hyperchromic effect suggests that compound **4** maintains its molecular integrity, while being effectively dispersed throughout the polymer matrix. The slight peak broadening observed in the drug-loaded nanogel, compared to the free drug, indicates the formation of a complex between compound **3** and the polymer chains through physical or chemical interactions.

The compound **4**-loaded nanogel exhibits unique spectral features that confirm its successful entrapment within the Cs/PVA matrix. The appearance of the characteristic absorption maximum, coupled with peaks compared to the free drug, provides evidence of the drug–polymer interactions. Furthermore, the maintenance of the spectral signature of the drug within the nanogel suggests that the incorporation process preserved the chemical structure of the drug, while achieving uniform distribution throughout the polymer network. These spectroscopic observations collectively demonstrate the

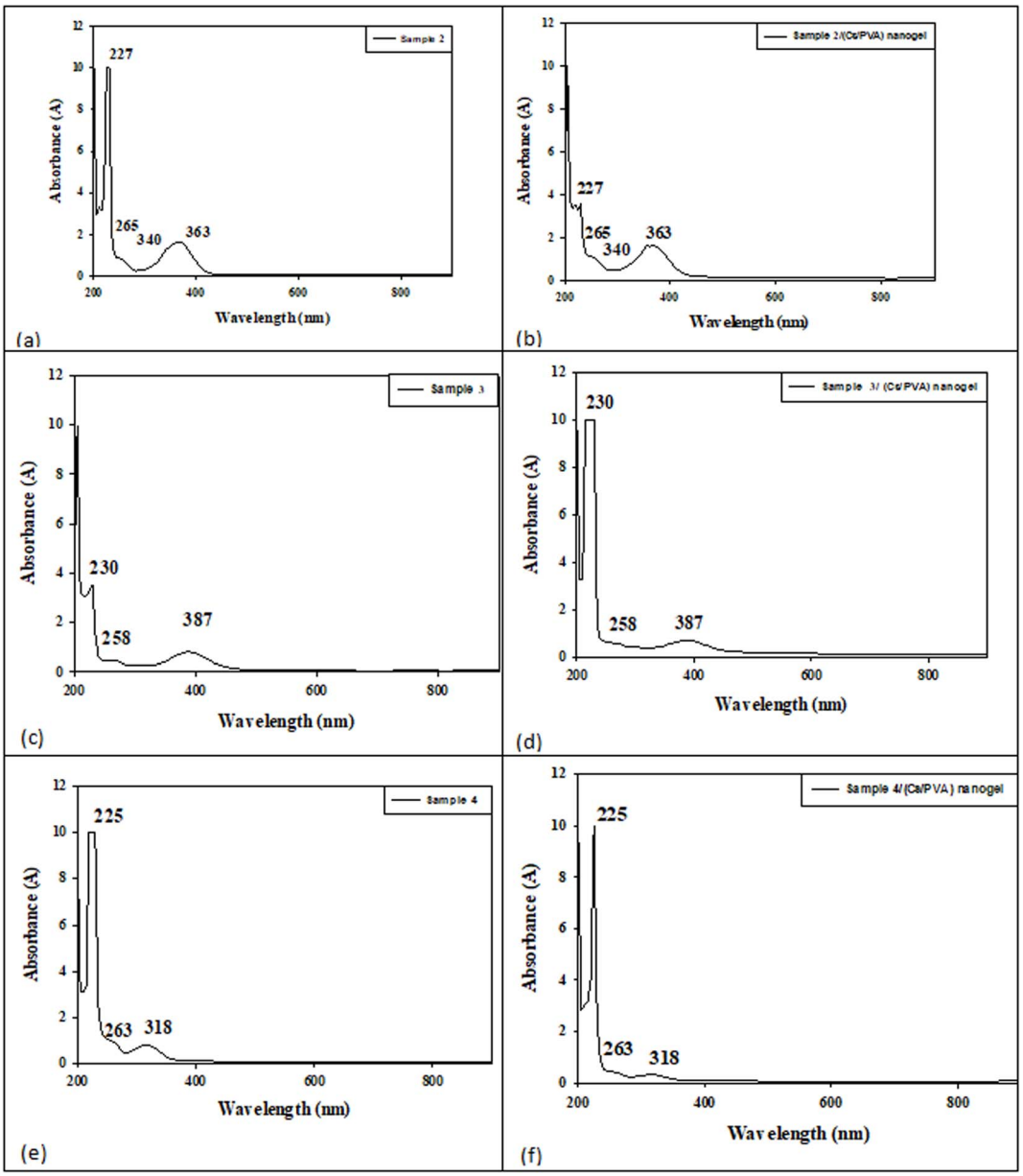

Fig. 2 The UV-Vis spectra of pure compounds **2** (a), **3** (c), **4** (e) and their Cs/PVA nanogels loaded with compounds **2** (b), **3** (d), and **4** (f). The distinct absorption peaks confirm the successful incorporation of each compound into the polymer matrix with characteristic spectral features for each derivative-loaded system.

successful loading of all three drugs into the Cs/PVA nanogel system, with each drug maintaining its chemical integrity, while forming stable interactions with the polymer matrix. The distinct spectral patterns serve as fingerprints for each drug-loaded system, confirming the effectiveness of the incorporation methodology.

2.2.2. Dynamic light scattering (DLS) analysis of drug-loaded Cs/PVA nanogels. The dynamic light scattering (DLS) analysis presented in Fig. 3 reveals significant insights into the physical characteristics and colloidal stability of the drug-loaded Cs/PVA nanogel systems. The results demonstrate distinct variations in particle size and surface charge properties among the three drug-loaded formulations.

In the case of the compound **2**-loaded Cs/PVA nanogel (Fig. 3a and b), the DLS measurements indicate a mean particle size of 612 nm with a relatively narrow size distribution, suggesting uniform particle formation. Its corresponding zeta potential value of −9.7 mV is particularly noteworthy, given that it exceeds the critical threshold of ±20 mV typically associated with colloidal stability. This strong negative surface charge indicates excellent electrostatic stabilization of the compound **2**-loaded nanogel particles, preventing their aggregation through electrostatic repulsion. The substantial negative charge likely resulted from the interaction between compound **2** and the polymer matrix, possibly due to the exposure of charged functional groups at the particle surface.

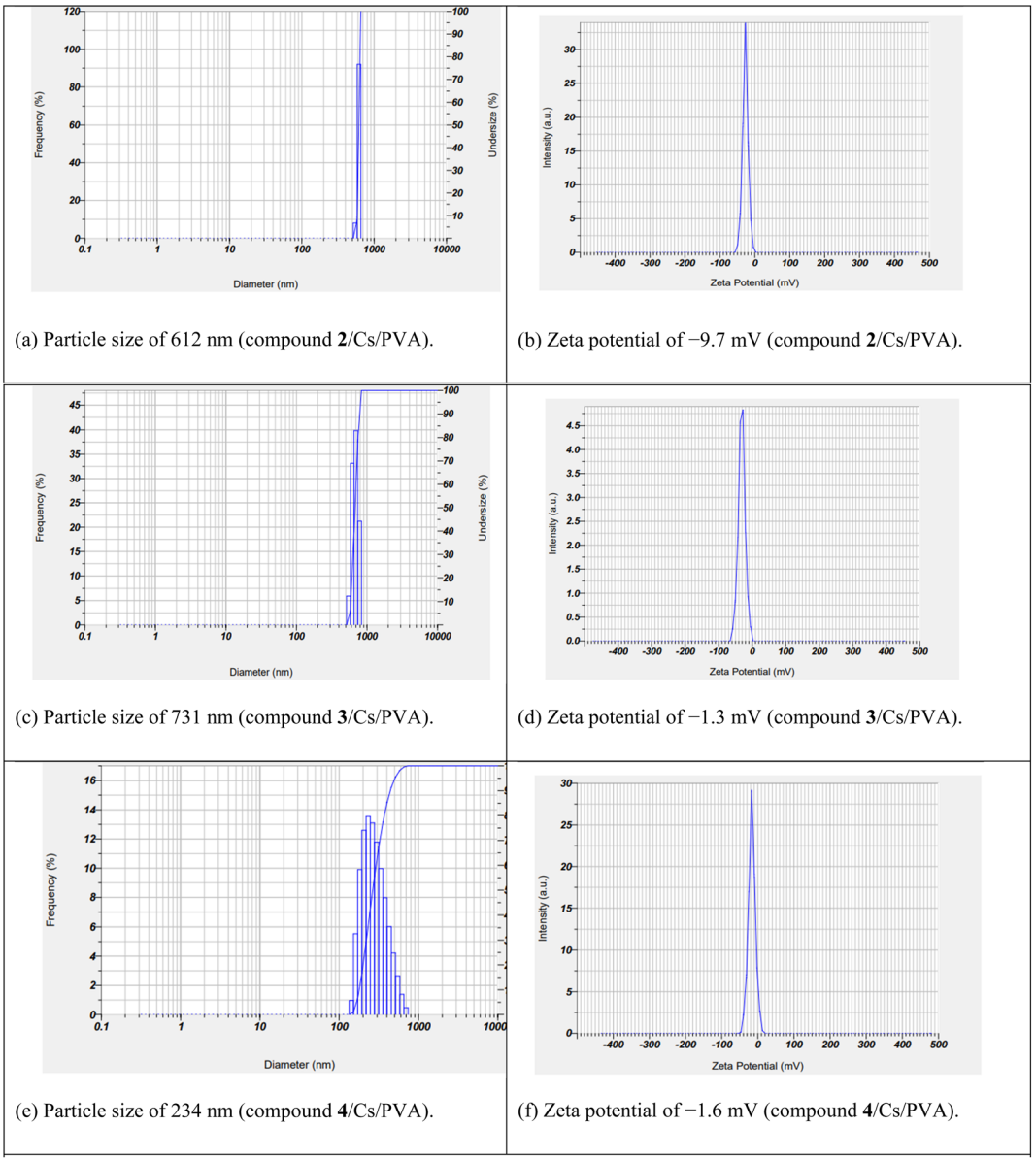

(a) Particle size of 612 nm (compound **2**/Cs/PVA). (b) Zeta potential of −9.7 mV (compound **2**/Cs/PVA).

(c) Particle size of 731 nm (compound **3**/Cs/PVA). (d) Zeta potential of −1.3 mV (compound **3**/Cs/PVA).

(e) Particle size of 234 nm (compound **4**/Cs/PVA). (f) Zeta potential of −1.6 mV (compound **4**/Cs/PVA).

Fig. 3 DLS results showing particle size distribution for Cs/PVA nanogels loaded with compounds **2** (a), **3** (c), **4** (e) and their zeta potential measurements for compounds **2** (b), **3** (d) and **4** (f).

The compound **3**-loaded Cs/PVA nanogel system (Fig. 3c and d) exhibited a larger mean particle size of 731 nm, suggesting that the incorporation of compound **3** led to greater particle expansion or different polymer chain arrangements. However, its measured zeta potential value of −1.3 mV indicates near-neutral surface charge, which could potentially lead to reduced colloidal stability compared to the compound **2**-loaded system. This near-neutral charge suggests that compound **3** might be primarily entrapped within the polymer matrix rather than contributing to surface charge properties.

Interestingly, the compound **4**-loaded Cs/PVA nanogel (Fig. 3e and f) showed the smallest particle size among all formulations of 234 nm. This significant reduction in particle size implies that compound **4** might influence the polymer chain organization during nanogel formation, possibly promoting more compact structures. The zeta potential value of −1.6 mV is similar to that of the compound **3**-loaded system, indicating minimal surface charge, which may necessitate additional stabilization strategies for long-term storage.

The variation in particle size (234–731 nm) across three compound-loaded systems suggests that drug physicochemical properties significantly influence the nanogel formation process and final structure. The substantially different zeta potential values, particularly the highly negative charge of the compound **2**-loaded system, indicate that drug incorporation not only affects the particle size but also the surface charge characteristics. These differences in physical properties may have important implications in the drug release kinetics,

cellular uptake, and overall therapeutic efficacy of the nanogel delivery systems.

Overall, the DLS results demonstrate successful drug incorporation with distinct effects on the nanogel properties, highlighting the need for formulation-specific optimization strategies to ensure the optimal stability and performance of each drug-loaded system.

2.2.3. Transmission electron microscopy (TEM) images of drug-loaded Cs/PVA nanogels. The transmission electron microscopy (TEM) images presented in Fig. 4 provide crucial insights into the morphological characteristics and internal structure of the drug-loaded Cs/PVA nanogel systems. The micrographs reveal distinct structural features specific to each drug-loaded formulation, confirming the successful drug incorporation and highlighting the influence of the different drugs on the nanogel morphology.

The TEM image of the compound **2**-loaded Cs/PVA nanogel (Fig. 4a) demonstrates spherical particles with well-defined boundaries and relatively uniform size distribution. The particles exhibited a characteristic core–shell structure, where the darker regions likely represent areas of higher electron density, suggesting concentrated drug localization within the polymer matrix. The observed particle size correlates well with the DLS measurements, showing particles in the range of approximately 600 nm. The surface texture appears slightly rough, indicating potential surface drug adsorption in addition to internal drug loading. The clear particle boundaries and absence of aggregation support the stability indicated by the strong negative zeta potential (−9.7 mV) observed in the DLS analysis.

In the case of the compound **3**-loaded Cs/PVA nanogel (Fig. 4b), its TEM micrograph reveals slightly larger particles with a more complex internal structure. Generally, the particles maintained a spherical morphology but showed increased size variability compared to the compound **2** system, consistent with the larger mean particle size (731 nm) measured by DLS. The internal contrast patterns suggest a more heterogeneous drug distribution within the polymer network, possibly due to the different drug–polymer interactions. Some particles exhibit slight deformation, which can be attributed to the lower surface charge stability indicated by the near-neutral zeta potential (−1.3 mV).

The TEM image of the compound **4**-loaded Cs/PVA nanogel (Fig. 4c) displays notably smaller particles with a more compact structure, supporting the DLS-measured size of 234 nm. These particles show a remarkably uniform size distribution and appear to have a more homogeneous internal structure compared to the other formulations. The smooth particle surface and clear boundaries indicate efficient drug encapsulation within the polymer matrix. Despite the near-neutral zeta potential (−1.6 mV), the particles maintained their individual integrity without significant aggregation, suggesting effective steric stabilization by the polymer network.

Across all three formulations, the TEM images confirmed the successful formation of nano-sized drug delivery systems with distinct morphological characteristics. The observed structural differences among the drug-loaded systems reflect the influence of the drug physicochemical properties on the nanogel formation and organization, providing valuable insights into the drug–polymer interactions and their potential implications for drug release behavior and therapeutic efficacy.

2.3. *In vitro* anti-proliferative activity

The anticancer activities of compounds **2**, **3**, and **4** and their nanogel preparations were evaluated on four cell lines, HepG2, A549, MCF-7 and HCT-116 (Table 1), using the MTT assay.[41–44] The cell line affected the most by our derivatives was A549. Compound **4** was the most active against the A549, HCT116, HepG2 and MCF-7 cancer cell lines with IC_{50} = 5.50, 9.77, 7.12 and 7.85 μM, respectively. The assessment of the cytotoxicity on the A549 cell line showed that compounds **2** and **3** with IC_{50} = 6.30 and 6.10, respectively, have high anticancer effects. Also, they showed good cytotoxicity against HCT-116 with IC_{50} = 10.60 and 11.00 μM, respectively. Furthermore, derivatives **2** and **3** showed high cytotoxic activities against HepG2 and MCF-

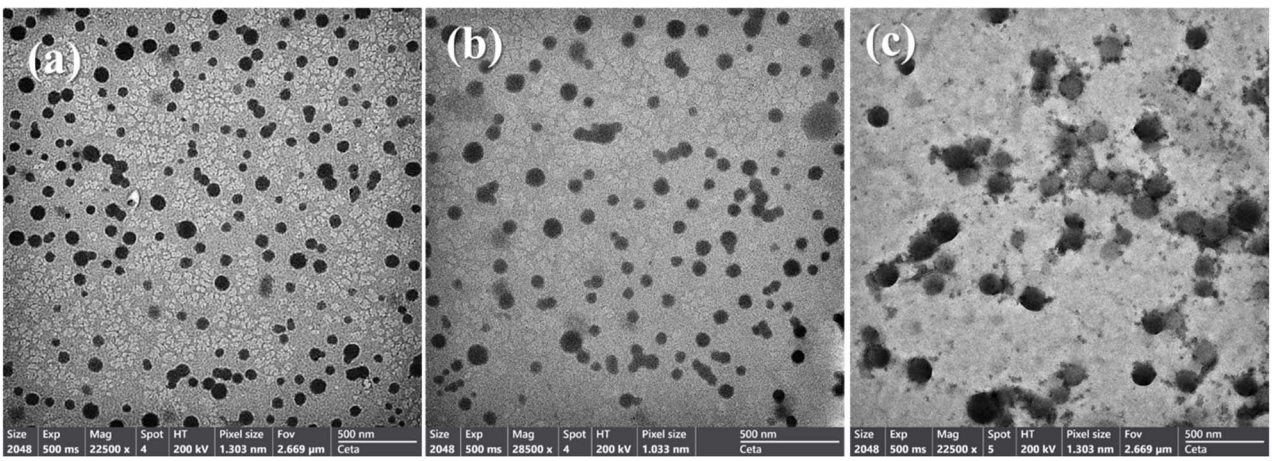

Fig. 4 TEM images of Cs/PVA nanogels loaded with compound **2** (a), compound **3** (b), and compound **4** (c). The micrographs reveal distinct particle morphologies and the internal structures, reflecting the effects of drug incorporation on nanogel formation and stability.

Table 1 *In vitro* cytotoxic activities of our compounds against A549, MCF-7, HepG2, HCT-116 and the VERO cell lines

	IC_{50}[a] (μM)				
Compound	A549	HCT116	HepG2	MCF-7	VERO
2	6.30 ± 0.5	10.60 ± 1.5	8.80 ± 0.5	8.30 ± 0.5	59.70 ± 2.9
2 (Nanogel)	4.28 ± 0.5	7.53 ± 1.5	4.90 ± 0.5	4.15 ± 0.5	50.25 ± 2.9
3	6.10 ± 0.5	11.00 ± 1.1	8.95 ± 0.5	8.65 ± 0.8	54.40 ± 2.9
3 (Nanogel)	4.05 ± 0.5	7.63 ± 1.1	4.95 ± 0.5	4.51 ± 0.8	48.29 ± 2.9
4	5.50 ± 0.5	9.77 ± 1.1	7.12 ± 0.5	7.85 ± 0.5	57.44 ± 2.9
4 (Nanogel)	3.75 ± 0.5	5.85 ± 1.1	3.56 ± 0.5	3.72 ± 0.5	49.68 ± 2.9
Doxorubicin	8.54 ± 0.8	8.07 ± 0.8	7.94 ± 0.6	6.75 ± 0.4	[b]NT

[a] IC_{50} values are the mean ± S.D. of three separate experiments. [b] NT = not tested.

7 with IC_{50} = 8.80 and 8.95 μM and 8.30 and 8.65 μM, respectively.

The nanogel as a drug delivery system enhanced the cytotoxic activities of our compounds. The nanogel for compound **2** showed enhanced cytotoxic activity against the A549, HCT116, HepG2 and MCF-7 cancer cell lines by 32.06%, 28.96%, 44.32% and 50.00% respectively. Moreover, the nanogel for compound **3** showed enhanced cytotoxic activity against the A549, HCT116, HepG2 and MCF-7 cancer cell lines by 33.61%, 30.64%, 44.69% and 47.86%, respectively. Furthermore, the nanogel for compound **4** showed enhanced cytotoxic activity against the A549, HCT116, HepG2 and MCF-7 cancer cell lines by 31.82%, 40.12%, 50.00% and 52.61%, respectively.

Moreover, the cytotoxicity of our derivatives **2**, **2 (nanogel)**, **3**, **3 (nanogel)**, **4** and **4 (nanogel)** was observed on VERO normal cell lines. The tested derivatives revealed good selectivity against cancer cells and low toxicity to VERO cells with IC_{50} values in the range of 48.29 to 59.70 μM. Derivatives **2**, **2 (nanogel)**, **3**, **3 (nanogel)**, **4** and **4 (nanogel)** were 9.48, 11.74, 8.92, 11.92, 10.44 and 13.25-fold more toxic to A549 cells than VERO normal cells, respectively. Uniformly, derivatives **2**, **2 (nanogel)**, **3**, **3 (nanogel)**, **4** and **4 (nanogel)** were consequently 5.63, 6.67, 4.95, 6.33, 5.88 and 8.49-fold more toxic to HCT-116 cells than in normal VERO cells, respectively. Furthermore, structures **2**, **2 (nanogel)**, **3**, **3 (nanogel)**, **4** and **4 (nanogel)** were 6.78, 10.26, 6.08, 9.76, 8.07 and 13.96-fold toxic to HepG-2 cells than ordinary VERO cells, respectively. Furthermore, products **2**, **2 (nanogel)**, **3**, **3 (nanogel)**, **4** and **4 (nanogel)** were 7.19, 12.11, 6.29, 10.71, 7.32 and 13.35-fold more toxic to MCF-7 cells than ordinary VERO cells, respectively.

2.4. *In vitro* DNA/methyl green assay

Synthesized derivatives **2**, **3**, **4** and their nanogel preparations were further evaluated for their DNA-binding affinities (Table 2) using methyl green dye.[45,46] Doxorubicin, as a powerful DNA intercalator, was incorporated as a positive control.

The tested derivatives showed very good DNA-binding affinities. The nanogels of compounds **4**, **2** and **3** presented the highest binding affinities respectively. These nanogels powerfully intercalated DNA at IC_{50} = 30.78, 32.40 and 34.55 μM, respectively. Moreover, compounds **4**, **2** and **3** demonstrated good DNA-binding affinities with IC_{50} = 35.95, 36.98 and 38.65 μM, respectively.

Table 2 DNA binding affinity and topo-II inhibition of our derivatives

Compound	DNA binding IC_{50} (μM)	Topo-II assay IC_{50} (μM)
2	36.98 ± 3.9	1.310 ± 0.40
2 (Nanogel)	32.40 ± 3.8	0.980 ± 0.40
3	38.65 ± 3.8	1.485 ± 0.40
3 (Nanogel)	34.55 ± 3.5	1.060 ± 0.40
4	35.95 ± 3.5	1.200 ± 0.40
4 (Nanogel)	30.78 ± 3.7	0.900 ± 0.40
Doxorubicin	31.27 ± 1.8	0.940 ± 0.40

2.5. *In vitro* topoisomerase II inhibitory activity

Our derivatives **2**, **3** and **4** were evaluated for their inhibition activities against the topo-II enzyme (Table 2).[45–47] The tested derivatives exhibited very good topo-II inhibition with IC_{50} = 0.900–1.485 μM, which is comparable with that by doxorubicin (IC_{50} = 0.94 μM). The obtained results were combined with the *in vitro* cytotoxic activities and DNA binding studies. Amongst them, the nanogels of compounds **4**, **3** and **2** were found to be the most powerful derivatives with very low IC_{50} = 0.900, 0.980 and 1.060 μM, respectively.

2.6. *In silico* ADMET profile

The highly active compounds **2**, **3** and **4** were *in silico* investigated by ADMET predictions. This was according to Lipinski's rule of five[48] and estimated using the pkCSM descriptor algorithm.[49] For good absorption, derivatives should follow at least three rules, including (i) H-bond acceptors must not exceed ten, (ii) molecular mass should be less than 500 u, (iii) log *P* should be less than five, and (iv) H-bond donors must not exceed five. In this study, although doxorubicin violates three of Lipinski's rules, our novel molecules **2**, **3** and **4** did not.

Our derivatives exhibited moderate human intestine absorption (43.746% to 58.002%), which indicates that they are capable of crossing diverse biological membranes[50] (Table 3). Our structures can enter the CNS (CNS permeability range: −2.612 to −3.228 (log PS)).

Table 3 ADMET profiles of our compounds **2**, **3**, and **4** and doxorubicin

Parameter	**2**	**3**	**4**	Doxorubicin sorafenib
Physicochemical properties				
Molecular weight (dalton (u))	377.36	413.306	429.418	543.525
log *P*	2.1915	1.9725	0.6512	0.0013
Rotatable bonds	5	6	5	5
Acceptors	7	10	8	12
Donors	2	2	4	6
Surface area (Å^2)	159.038	165.778	169.652	222.081
Absorption				
Water solubility (log mol L^{-1})	−2.811	−3.03	−3.058	−2.915
Human intest. absorption (%)	58.002	54.673	43.746	62.372
Inhibitor of P-glycoprotein II	Not	Not	Not	Not
Substrate for P-glycoprotein	Not	Yes	Yes	Yes
Inhibitor of P-glycoprotein I	Not	Not	Not	Not
Distribution				
BBB permeability (conc. in Brain/Blood (log BB))	−1.014	−1.845	−1.607	−1.379
CNS permeability (Permeability-Surface area (log PS))	−2.612	−2.952	−3.228	−4.307
Metabolism				
Inhibition of CYP3A4	Not	Not	Not	Not
Inhibition of CYP2D6	Not	Not	Not	Not
Inhibition of CYP2C9	Not	Not	Not	Not
Inhibition of CYP2C19	Not	Not	Not	Not
Inhibition of CYP1A2	Not	Not	Not	Not
CYP3A4 substrate	Not	Not	Not	Not
CYP2D6 substrate	Not	Not	Not	Not
Excretion				
Clearance (log mL min^{-1} kg^{-1})	0.11	−0.072	−0.459	0.987
Toxicity				
Acute toxic activity (LD_{50}) (mol kg^{-1})	2.547	2.171	2.305	2.408
Chronic toxicity activity (LOAEL) (log mg per kg_bw per day)	2.234	1.867	1.871	3.339
Human max. tolerated dose (log mg per kg per day)	0.582	0.288	0.308	0.081
Hepatotoxic effect	No	No	Yes	Yes

Generally, doxorubicin and our derivatives **2**, **3** and **4** did not inhibit drug metabolism through CYP3A4 inhibition. The total clearance gives an idea about predicted elimination, which detects the dosing interval. Doxorubicin exhibited greater clearance rates than our derivatives. Doxorubicin might be eliminated more speedily, and thus shorter dosing intervals are needed. In contrast to doxorubicin, our derivatives exhibited slow clearance rates, which represent prolonged half-life and broader dosing windows. Hepatotoxicity was displayed by compound **4** and doxorubicin, but not by **2** and **3**. Doxorubicin showed the lowest maximum tolerated dose. However, the maximum tolerated doses for our structures were higher. Finally, the acute toxic doses of doxorubicin and our compounds were approximately equal. Moreover, the oral chronic toxic dose of doxorubicin was higher than our compounds. These data demonstrate that our compounds have a respectable therapeutic index.

3. Conclusion

In summary, our pyrazole derivatives **2** and **3** and pyrimidine derivative **4** and their nanogels as drug delivery systems were designed, synthesized and investigated for their anticancer activities against the HepG2, HCT-116, MCF-7 and A549 cell lines using doxorubicin as a reference cytotoxic drug. The most affected cell line by our derivatives was A549. Compound **4** was the most active against the A549, HCT116, HepG2 and MCF-7 cancer cell lines with IC_{50} = 5.50, 9.77, 7.12 and 7.85 μM, respectively. Assessment of their cytotoxicity on the A549 cell line showed that compounds **2** and **3** with IC_{50} = 6.30 and 6.10, respectively, showed high anticancer effects. Also, against the HCT-116 cancer cell line, they showed good cytotoxicity with IC_{50} = 10.60 and 11.00 μM, respectively. Furthermore, derivatives **2** and **3** exhibited high cytotoxic activities against HepG2 and MCF-7 with IC_{50} = 8.80 and 8.95 μM and 8.30 and 8.65 μM, respectively. The nanogels as drug delivery systems enhanced the cytotoxic activities of our compounds. The nanogel of compound **2** showed enhanced cytotoxic activity against the A549, HCT116, HepG2 and MCF-7 cancer cell lines by 32.06%, 28.96%, 44.32% and 50.00%, respectively. Moreover, the nanogel of compound **3** showed enhanced cytotoxic activity against the A549, HCT116, HepG2 and MCF-7 cancer cell lines by 33.61%, 30.64%, 44.69% and 47.86%, respectively.

Furthermore, the nanogel for compound **4** showed enhanced cytotoxic activity against the A549, HCT116, HepG2 and MCF-7 cancer cell lines by 31.82%, 40.12%, 50.00% and 52.61%, respectively.

Moreover, the cytotoxicity activities of our derivatives **2**, **2 (nanogel)**, **3**, **3 (nanogel)**, **4** and **4 (nanogel)** were observed on the VERO normal cell line. The tested derivatives exhibited good selectivity against cancer cells and low toxicity to VERO cells with IC_{50} values in the range of 48.29 to 59.70 μM. Derivatives **2**, **2 (nanogel)**, **3**, **3 (nanogel)**, **4** and **4 (nanogel)** were 9.48, 11.74, 8.92, 11.92, 10.44 and 13.25-fold more toxic to A549 cells than VERO normal cells, respectively. Similarly, derivatives **2**, **2 (nanogel)**, **3**, **3 (nanogel)**, **4** and **4 (nanogel)** were 5.63, 6.67, 4.95, 6.33, 5.88 and 8.49-fold more toxic to HCT-116 cells than normal VERO cells. Furthermore, structures **2**, **2 (nanogel)**, **3**, **3 (nanogel)**, **4** and **4 (nanogel)** were 6.78, 10.26, 6.08, 9.76, 8.07 and 13.96-fold more toxic to HepG-2 cells than ordinary VERO cells. Furthermore, products **2**, **2 (nanogel)**, **3**, **3 (nanogel)**, **4** and **4 (nanogel)** were 7.19, 12.11, 6.29, 10.71, 7.32 and 13.35-fold more toxic to MCF-7 cells than ordinary VERO cells. The nanogel of compounds **4**, **2** and **3** displayed the highest DNA binding affinities at decreased IC_{50} values of 30.78, 32.40 and 34.55 μM, respectively. Moreover, compounds **4**, **2** and **3** exhibited good DNA-binding affinities with IC_{50} values of 35.95, 36.98 and 38.65 μM, respectively. Also, the tested compounds exhibited very good topo-II inhibitory activities with IC_{50} values in the range of 0.900 to 1.485 μM in comparison to doxorubicin (IC_{50} = 0.94 μM). Furthermore, the ADMET profiles of our compounds were calculated and compared to doxorubicin as a reference drug. Our derivatives showed good ADMET profiles. Although doxorubicin violates three of Lipinski's rules, our derivatives did not violate any. Also, doxorubicin exhibited greater clearance rates than our derivatives. Doxorubicin may be eliminated more speedily, and thus needs shorter dosing intervals. In contrast to doxorubicin, our derivatives exhibited slow clearance rates, which represent prolonged half-life and broader dosing windows.

4. Experimental section

4.1. Chemistry

4.1.1. General. ^{1}H NMR and ^{13}C NMR spectra were measured on Varian Mercury 300 MHz and 100 MHZ-NMR spectrometers, respectively. The starting material 2-((1-cyano-2-ethoxy-2-oxoethyl)diazenyl)benzoic acid **1** was prepared using a procedure reported in the literature.[39,40]

4.1.2. General procedure for synthesis of target compounds (2–4). A solution of compound **2** (2.61 g, 0.01 mol) in DMF (20 mL) was refluxed for 8–20 h with cinnamohydrazide (1.62 g, 0.01 mol), 2,4-dinitrophenyl hydrazine (1.98 g, 0.01 mol) and/or sulphaguanidine (2.14 g, 0.1 mol). After cooling, the mixture was poured into ice water (100 mL), and the formed solid was filtered, washed three times with ethanol (10 mL) and recrystallized from the appropriate solvent to give the corresponding compounds **2–4**, respectively.

4.1.2.1. 2-((3-Amino-1-cinnamoyl-5-oxo-4,5-dihydro-1H-pyrazol-4-yl)diazenyl)benzoic acid (2). Brown crystals from ethanol; m.p. > 300 °C; IR (cm^{-1}) υ: 3397 (OH), 3312, 3275 (NH_2), 1735, 1682, 1649 (C=O), 1599 (C=N), 1547 (N=N). ^{1}H-NMR (300 MHz, DMSO-d_6) δ (ppm): 1.93 (s, 1H, –N=N–CH), 6.96–8.65 (m, 13H, Ar–H and NH_2, D_2O exchangeable), 15.45 (s, 1H, OH, D_2O exchangeable). ^{13}C-NMR (300 MHz, DMSO-d_6) δ (ppm): 60.5, 117.5, 118.3, 120.8, 120.9, 121.0, 123.3, 124.5, 131.7, 131.7, 131.8, 131.9, 132.2, 133.1, 144.3, 144.6, 150.3, and 160.1. MS (*m*/*z*): 377 (M^+, 10.16%); Anal. Calcd for $C_{19}H_{15}N_5O_4$ (377): C, 60.48; H, 3.98; N, 18.57, found: C, 60.30; H, 4.04; N, 18.66.

4.1.2.2. 2-((3-Amino-1-(2,4-dinitrophenyl)-5-oxo-4,5-dihydro-1H-pyrazol-4-yl)diazenyl)benzoic acid (3). Brown crystals from methanol; m.p. > 300 °C; IR (cm^{-1}) υ: 3361–3200 (broad, OH, NH_2), 1696, 1674 (C=O), 1602 (C=N), 1548 (N=N). ^{1}H-NMR (300 MHz, DMSO-d_6) δ (ppm): 2.74 (s, 1H, –N=N–CH), 7.39–8.01 (m, 9H, Ar–H and NH_2, D_2O exchangeable), 14.52 (s, 1H, OH, D_2O exchangeable). ^{13}C-NMR (300 MHz, DMSO-d_6) δ (ppm): 67.9, 127.3, 131.5, 131.6, 132.0, 132.1, 148.4, 166.9, and 168.4. MS (*m*/*z*): 413 (M^+, 19.75%); Anal. Calcd for $C_{16}H_{11}N_7O_7$ (413): C, 46.49; H, 2.66; N, 23.73, found: C, 46.55; H, 2.59; N, 23.88.

4.1.2.3. 2-((4-Amino-2-(((4-aminophenyl)sulfonyl)imino)-6-oxo-1,2,5,6-tetrahydropyrimidin-5-yl)diazenyl)-benzoic acid (4). Orange crystal from ethanol; m.p. > 300 °C; IR (cm^{-1}) υ: 3297 (NH_2), 3099, 3072 (NH), 1688, 1666 (C=O), 1601 (C=N), 1553 (N=N). ^{1}H-NMR (300 MHz, DMSO-d_6) δ (ppm): 1.74 (s, 1H, –N=N–CH), 6.93–8.00 (m, 12H, Ar–H and $2NH_2$, D_2O exchangeable), 9.64 (s, 1H, NH, D_2O exchangeable), 15.46 (s, 1H, OH, D_2O exchangeable). ^{13}C-NMR (300 MHz, DMSO-d_6) δ (ppm): 60.6, 102.0, 115.0, 115.3, 118.6, 122.7, 129.4, 131.3, 133.1, 143.4, 150.8, 154.0, 160.0, 163.9, and 169.3. MS (*m*/*z*): 429 (M^+, 12.28%); Anal. Calcd for $C_{17}H_{15}N_7O_5S$ (429): C, 47.55; H, 3.49; N, 22.84; S, 7.46, found: C, 47.67; H, 3.33; N, 22.71; S, 7.37.

4.2. Nanogel preparation

4.2.1. Materials and sources. Low molecular weight chitosan (Cs) was purchased from Sigma-Aldrich (St. Louis, MO, USA). Polyvinyl alcohol (PVA, 87–89% hydrolyzed) was obtained from Merck KGaA (Darmstadt, Germany). Glutaraldehyde solution (GA, 25% in H_2O), glacial acetic acid (≥99.7%), ammonium persulfate (APS, ≥98%), and *N*,*N*′-methylenebisacrylamide (MBA) were all acquired from Sigma-Aldrich. Sodium hydroxide (NaOH) pellets and hydrochloric acid (HCl, 37%) were purchased from Fisher Scientific (Hampton, NH, USA). All chemicals were of analytical grade and used without further purification. Deionized water was used throughout the experiments.

4.2.2. Preparation of chitosan/polyvinyl alcohol (Cs/PVA) nanogel. The preparation of the Cs/PVA nanogel began with the separate preparation of the polymer solutions. For the chitosan solution, 2.0 g of chitosan was carefully weighed and dissolved in 100 mL of 1.5% (v/v) acetic acid solution.[51] The mixture was subjected to continuous magnetic stirring at 500 rpm for 0.5 h at room temperature (25 °C) until a clear, homogeneous solution was obtained. The pH of the resulting chitosan solution was measured and adjusted to 5.8 *via* the dropwise addition of 0.1 M NaOH solution under constant monitoring using a calibrated pH meter. The PVA solution was

prepared by dissolving 7.5 g of PVA in 100 mL of distilled water. The mixture was heated to 80 °C in a water bath equipped with a temperature controller, maintaining continuous stirring at 600 rpm for 1.5 h to ensure the complete dissolution of the PVA. Then, the solution was allowed to cool to room temperature while maintaining gentle stirring at 200 rpm to prevent premature gelation. The blending process was initiated by slowly adding the prepared chitosan solution to the PVA solution at a rate of approximately 2 mL min^{-1} under vigorous stirring at 700 rpm. The combined solution was maintained under continuous stirring for 30 min at room temperature to ensure thorough mixing of the two polymers. For the cross-linking reaction, 0.3 mL of glutaraldehyde solution was added dropwise to the polymer mixture, followed by the addition of 0.15 g of APS (dissolved in 5 mL of distilled water) as an initiator. For additional stabilization, 0.03 g of MBA was incorporated into the mixture. The pH of the final mixture was carefully maintained at 6.0 ± 0.2 throughout the process using 0.1 M HCl or 0.1 M NaOH as needed. The cross-linking reaction was carried out by heating the mixture to 65 °C in a temperature-controlled water bath for 1.5 h under gentle stirring at 300 rpm. Then, the resulting nanogel was allowed to cool naturally to room temperature. The purification process involved the dialysis of the nanogel against distilled water using a dialysis membrane (molecular weight cut-off 12–14 kDa) for 36 h, with the dialysis medium being changed every 12 h to ensure complete removal of the unreacted components and byproducts. Alternatively, the nanogel was purified through repeated centrifugation at 4000 rpm for 10-min cycles, washing with distilled water between each cycle until the supernatant became clear.

The final purified nanogel was stored in a sterile glass container at 4 °C for subsequent characterization and application. The entire preparation process was conducted under controlled laboratory conditions with careful attention to maintaining sterility and precise reaction parameters throughout each step.

4.2.3. Drug loading protocol for Cs/PVA nanogel systems. The incorporation of compound **2** into the Cs/PVA nanogel system was performed using a precise solvent-based loading method.[52] Initially, 100 mg of compound **2** was accurately weighed using an analytical balance and completely dissolved in 10 mL of dimethyl sulfoxide (DMSO) under gentle magnetic stirring at 300 rpm for 15 minutes at room temperature (25 °C) to ensure complete dissolution. The resulting drug solution (10 mg mL^{-1}) was then gradually incorporated into 10 mL of the prepared Cs/PVA nanogel suspension using a dropwise addition method at approximately 1 mL min^{-1} rate under continuous stirring at 500 rpm. The incorporation process was conducted at room temperature, and the mixture was further stirred for 2 hours to ensure uniform drug distribution throughout the nanogel matrix. The final drug-loaded nanogel suspension contained compound **2** at a concentration of 5 mg mL^{-1}. The mixture was then subjected to gentle vacuum treatment for 30 minutes to remove trapped air bubbles and ensure homogeneous drug distribution. The other two compounds (**3** and **4**) have cooperated, as mentioned in compound **2**. For all three drug-loaded nanogel systems, the final preparations were stored in amber glass vials at 4 °C under dark conditions to protect from light degradation. Each drug-loaded nanogel system was characterized within 24 hours of preparation to verify drug-loading efficiency and uniform distribution. The drug-loaded nanogels were monitored for any signs of phase separation or drug precipitation during storage. All incorporation procedures were performed under aseptic conditions using sterile equipment and materials to maintain the integrity of the final drug-delivery systems. The incorporation process for each drug was performed separately to avoid any potential drug–drug interactions and to ensure accurate loading concentrations for each system.

4.2.4. *In vitro* cytotoxic activity. Cancer cells including HepG2, HCT-116, A549, and MCF-7 and VERO normal cells were obtained from ATCC (the American Type Culture Collection) in Manassas, USA. These cells were cultured in the appropriate growth medium, namely Roswell Park Memorial Institute medium (RPMI 1640), complemented with 10% heat-inactivated fetal bovine serum, 100 units per mL of penicillin, and 100 mg mL^{-1} of streptomycin. The cell cultures were kept in a humidified atmosphere with 5% (v/v) CO_2 at 37 °C. Following the MTT (3-[4,5-dimethylthiazole-2-yl]-2,5-diphenyltetrazolium bromide) process,[41–44] cytotoxicity valuations were performed.

Cell lines from diverse cancers, in the active proliferation phase, were exposed to trypsinization, quantification, and then seeded at appropriate densities (ranging from 2000 to 1000 cells per 0.33 cm^2 well) in 96-well microtiter plates. Consequently, these cells were incubated for 24 h at 37 °C in a humid location. Then, the cells were exposed for a 72 h to variable compound concentrations (0.1, 10, 100, and 1000 μM).

The MTT procedure was performed to assess the treated cells viability as follows: the culture media were aspirated, and then the cells were incubated with 5% MTT solution (200 μL) in each well (Sigma Aldrich, MO). The cells were left for 2 h to convert the MTT dye into colored-insoluble formazan crystals. Then, the residual MTT solution was discarded, and the formazan crystals were dissolved for 30 min in 200 μL of acidified isopropanol in each well. This technique was performed at room temperature under continuous shaking using a MaxQ 2000 plate shaker (Thermo Fisher Scientific Inc., MI) and with the plates covered in aluminum foil. Using a Stat FaxR 4200 plate reader (Awareness Technology, Inc., FL), the absorbance was measured at 570 nm. Using the GraphPad Prism Version 5 software (Graph Pad Software Inc., CA), the cell viability in comparison to the control was expressed as a percentage, and the IC_{50} (half-maximum inhibitory concentration of cell proliferation) was obtained.

4.2.5. DNA/methyl green assay. Our derivatives were additionally assessed for their affinity towards DNA binding. Doxorubicin was used as the positive control DNA intercalator. In this assessment, methyl green dye can form a reversible colored DNA/methyl green complex. At neutral pH, this complex remained stable. Upon the addition of intercalating agents, the methyl green is replaced in DNA with the addition of H_2O molecules to form the colorless carbinol, resulting in

a remarkable decrease in spectrophotometric absorbance.[45,46] The variance between free carbinol and DNA/methyl green complex (ΔA value) affords the simplest means for identifying the relative DNA-binding strength and affinities. Using the GraphPad Prism 5.0 software, IC_{50} was obtained. The technique was performed as follows. A mixture of methyl green (20 mg) and calf thymus DNA (10 mg) (Sigma-Aldrich) in 100 mL of 0.05 M Tris–HCl buffer (pH 7.5) containing 7.5 mM $MgSO_4$ was prepared. Then, the mixture was stirred at 37 °C for 24 h. The test samples were dissolved in ethanol and dispensed into wells of a 96-well microtiter tray at a concentration of 10, 100 and 1000 μM. The extra solvent was discarded per well, under vacuum followed by the addition of 200 μL of solution of the DNA/methyl green. The test samples were incubated at room temperature in the dark. The absorbance of each sample was measured at 642.5–645 nm after 24 h. The results were normalized and corrected for early absorbance as the percentage of the untreated DNA/methyl green absorbance reading.

4.2.6. *In silico* ADMET analysis. The ADMET (absorption, distribution, metabolism, excretion, and toxicity) predictions of the derivatives were calculated using the pkCSM descriptor algorithm at **https://biosig.lab.uq.edu.au/pkcsm/prediction**. Firstly, the established derivatives were hand drawn, and their energy minimizations were performed in accordance with the preparation of small molecule protocol. To calculate different descriptors for a compound, the ADMET descriptor protocol was applied. This prediction helped in understanding the safety and pharmacokinetic profiles of the compounds, which are vital for drug evaluation and development. These descriptors afford visions into how these compounds are probably metabolized, distributed, absorbed, and excreted, and any possible toxicity related to them.

Data availability

The data supporting this article have been included as part of the ESI.†

Conflicts of interest

The authors declare no conflicts of interest.

References

1 L. Strekowski and B. Wilson, *Mutat. Res.*, 2007, **623**(1–2), 3.
2 A. Paul and S. Bhattacharya, *Curr. Sci.*, 2012, **102**, 212.
3 C. Avendano and J. Menéndez, *Medicinal Chemistry of Anticancer Drugs*, Elsevier, 2nd edn, 2008, p. 199.
4 G. Minotti, P. Menna, E. Salvatorelli, G. Cairo and L. Gianni, *Pharmacol. Rev.*, 2004, **56**, 185.
5 F. Gago, *Methods*, 1998, **14**, 277.
6 A.-G. A. El-Helby, R. R. A. Ayyad, H. Sakr, K. El-Adl, M. M. Ali and F. Khedr, *Arch. Pharm.*, 2017, **350**(12), 1, DOI: **10.1002/ardp.201700240**.
7 M. K. Goftar, *et al.*, DNA intercalators and using them as anticancer drugs, *Int. J. Adv. Biol. Biomed. Res.*, 2014, **2**(3), 811–822.
8 M. Sirajuddin, S. Ali and A. Badshah, *J. Photochem. Photobiol., B*, 2013, **124**, 1, DOI: **10.1016/j.jphotobiol.2013.03.013**.
9 A. Soni, P. Khurana, T. Singh and B. Jayaram, *Bioinformatics*, 2017, **33**(10), 1488, DOI: **10.1093/bioinformatics/btx006**.
10 S. Takenaka and M. Takagi, *Bull. Chem. Soc. Jpn.*, 1999, **72**, 327.
11 A. Chilin, G. Marzaro, C. Marzano, L. Dalla Via, M. G. Ferlin, G. Pastorini and A. Guiotto, *Bioorg. Med. Chem.*, 2009, **17**, 523.
12 L. F. Liu, *Annu. Rev. Biochem.*, 1989, **58**, 351.
13 T. D. Shenkenberg and D. D. Von Hoff, *Ann. Intern. Med.*, 1986, **105**, 67.
14 A. Garofalo, L. Goossens, B. Baldeyrou, A. Lemoine, S. Ravez, P. Six, M.-H. David-Cordonnier, J.-P. Bonte, P. Depreux, A. Lansiaux and J.-F. Goossens, *J. Med. Chem.*, 2010, **53**(22), 8089, DOI: **10.1021/jm1009605**.
15 J. Feng, H. Qi, X. Sun, S. Feng, Z. Liu, Y. Song and X. Qiao, Synthesis of Novel Pyrazole Derivatives as Promising DNA-Binding Agents and Evaluation of Antitumor and Antitopoisomerases I/II Activities, *Chem. Pharm. Bull.*, 2018, **66**(11), 1065–1071, DOI: **10.1248/cpb.c18-00546**.
16 J. L. Nitiss, Targeting DNA topoisomerase II in cancer chemotherapy, *Nat. Rev. Cancer*, 2009, **9**(5), 338–350, DOI: **10.1038/nrc2607**.
17 S. A. Rizvi and A. M. Saleh, Applications of nanoparticle systems in drug delivery technology, *Saudi Pharm. J.*, 2018, **26**(1), 64–70.
18 X. Zhang, *et al.*, Cetuximab-modified silica nanoparticle loaded with ICG for tumor-targeted combinational therapy of breast cancer, *Drug Delivery*, 2019, **26**(1), 129–136.
19 E. Roduner, Size matters: why nanomaterials are different, *Chem. Soc. Rev.*, 2006, **35**(7), 583–592.
20 E. Kohli, H. Y. Han, A. D. Zeman and S. V. Vinogradov, Formulations of biodegradable Nanogel carriers with 5'-triphosphates of nucleoside analogs that display a reduced cytotoxicity and enhanced drug activity, *J. Controlled Release*, 2007, **121**(1–2), 19–27, DOI: **10.1016/j.jconrel.2007.04.007**.
21 V. P. Torchilin, Multifunctional nanocarriers, *Adv. Drug Delivery Rev.*, 2006, **58**(14), 1532–1555, DOI: **10.1016/j.addr.2006.09.009**.
22 K. El-Adl, H. Sakr, M. Nasser and F. M. A. Shoman, *Arch. Pharm.*, 2020, e2000079, DOI: **10.1002/ardp.202000079**.
23 K. El-Adl, A.-G. A. El-Helby, H. Sakr and S. S. A. El-Hddad, *Arch. Pharm.*, 2020, e2000068, DOI: **10.1002/ardp.202000068**.
24 K. El-Adl, A. A. El-Helby, H. Sakr, I. H. Eissa, S. S. A. El-Hddad and F. M. A. Shoman, *Bioorg. Chem.*, 2020, **102**, 104059, DOI: **10.1016/j.bioorg.2020.104059**.
25 A. M. Sayed, F. A. Taher, M. R. K. Abdel-Samad, M. S. A. El-Gaby, K. El-Adl and N. M. Saleh, *Bioorg. Chem.*, 2021, **108**, 104669, DOI: **10.1016/j.bioorg.2021.104669**.
26 M. H. El-Shershaby, A. Ghiaty, A. H. Bayoumi, H. E. A. Ahmed, M. S. El-Zoghbi, K. El-Adl and

H. S. Abulkhair, *New J. Chem.*, 2021, **45**, 11136, DOI: 10.1039/D1NJ00710F.

27 A. A. El-Helby, H. Sakr, R. R. A. Ayyad, K. El-Adl, M. M. Ali and F. Khedr, *Anti-Cancer Agents Med. Chem.*, 2018, **18**(8), 1184, DOI: 10.2174/1871520618666180412123833.

28 K. El-Adl, A. -H. Abdel-Rahman, A. M. Omar, M. Alswah and N. M. Saleh, *Arch. Pharm.*, 2021, e2100237, DOI: 10.1002/ardp.202100237.

29 A. M Sayed, F. A. Taher, M. R. K. Abdel-Samad, M. S. A. El-Gaby, K. El-Adl and N. M. Saleh, *Bioorg. Chem.*, 2021, **108**, 104669, DOI: 10.1016/j.bioorg.2021.104669.

30 N. M. Saleh, A. A.-H. Abdel-Rahman, A. M. Omar, M. M. Khalifa and K. El-Adl, *Arch. Pharm.*, 2021, **354**, e2100085, DOI: 10.1002/ardp.202100085.

31 K. El-Adl, H. Sakr, M. Nasser, M. Alswah and F. M. A. Shoman, *Arch. Pharm.*, 2020, **353**, e2000079, DOI: 10.1002/ardp.202000079.

32 N. M. Saleh, M. S. A. El-Gaby, K. El-Adl and N. E. A. Abd El-Sattar, *Bioorg. Chem.*, 2020, **104**, 104350, DOI: 10.1016/j.bioorg.2020.104350.

33 F. Khedr, M. -K. Ibrahim, I. H. Eissa, H. S. Abulkhair and K. El-Adl, *Arch. Pharm.*, 2021, e2100201, DOI: 10.1002/ardp.202100201.

34 K. El-Adl, M.-K. Ibrahim, F. Khedr, H. S. Abulkhair and I. H. Eissa, *Arch. Pharm.*, 2021, **354**, e2000219, DOI: 10.1002/ardp.202000219.

35 K. El-Adl, A. A. El-Helby, H. Sakr and A. Elwan, *Bioorg. Chem.*, 2020, **105**, 104399, DOI: 10.1016/j.bioorg.2020.104399.

36 K. El-Adl, A. A. El-Helby, H. Sakr and A. Elwan, *New J. Chem.*, 2021, **45**, 881, DOI: 10.1039/D0NJ02990D.

37 N. E. A. Abd El-Sattar, K. El-Adl, M. A. El-Hashash, S. A. Salama and M. M. Elhady, *Bioorg. Chem.*, 2021, **22**(115), 105186, DOI: 10.1016/j.bioorg.2021.105186.

38 K. El-Adl, M.-K. Ibrahim, M. S. I. Alesawy and I. H. Eissa, *Bioorg. Med. Chem.*, 2021, **30**, 115958, DOI: 10.1016/j.bmc.2020.115958.

39 M. M. Mashaly, A. T. Ramadan, B. A. El-Shetary and A. K. Dawoud, Synthesis and Characterization of New Transition and Actinide Metal Complexes of a Hydrazone Ligand. Mixed-Ligand Complexes, Pyrolysis Products, and Biological Activity, *Synth. React. Inorg. Met.-Org. Chem.*, 2004, **34**(8), 1319–1348.

40 K. E. Anwer, S. S. A. El-Hddad, N. E. A. Abd El-Sattar, A. El-Morsy, F. Khedr, S. Mohamady, D. E. Keshek, S. A. Salama, K. El-Adl and N. S. Hanafy, Five and six membered heterocyclic rings endowed with azobenzene as dual EGFRT790M and VEGFR-2 inhibitors: design, synthesis, *in silico* ADMET profile, molecular docking, dynamic simulation and anticancer evaluations, *RSC Adv.*, 2023, **13**(50), 35321–35338, DOI: 10.1039/d3ra06614b.

41 T. Mosmann, Rapid colorimetric assay for cellular growth and survival: application to proliferation and cytotoxicity assays, *J. Immunol. Methods*, 1983, **65**(1–2), 55–63.

42 F. M. Freimoser, C. A. Jakob, M. Aebi and U. Tuor, The MTT [3-(4,5-Dimethylthiazol-2-yl)-2,5-Diphenyltetrazolium Bromide] Assay Is a Fast and Reliable Method for Colorimetric Determination of Fungal Cell Densities, *Appl. Environ. Microbiol.*, 1999, **65**(8), 3727–3729.

43 K. El-Adl, M.-K. Ibrahim, M. S. I. Alesawy and I. H. Eissa, [1,2,4]Triazolo[4,3-c]quinazoline and bis([1,2,4]triazolo)[4,3-a:4′,3′-c]quinazoline derived DNA intercalators: Design, synthesis, *in silico* ADMET profile, molecular docking and anti-proliferative evaluation studies, *Bioorg. Med. Chem.*, 2021, **30**, 115958, DOI: 10.1016/j.bmc.2020.115958.

44 K. El-Adl, M. M. Ghobashy, A. F. M. Ismail, A. El-morsy and N. A. Shoman, Radiation synthesis and characterization of pH-Responsive sodium Alginate/Poly(acrylic acid) nanogel loaded with ferulic acid for anticancer drug delivery, *Mater. Chem. Phys.*, 2024, **322**, 129564, DOI: 10.1016/j.matchemphys.2024.129564.

45 A. M. Soliman and A. A. Amer, Synthesis and Antimicrobial Activity of Some Novel Quinoxalines, *Synth. Commun.*, 2012, **42**(10), 1401–1410, DOI: 10.1080/00397911.2010.537802.

46 K. El-Adl, A. A. El-Helby, H. Sakr and A. Elwan, Design, synthesis, molecular docking and anti-proliferative evaluations of [1,2,4]triazolo[4,3-a]quinoxaline derivatives as DNA intercalators and Topoisomerase II inhibitors, *Bioorg. Chem.*, 2020, **105**, 104399, DOI: 10.1016/j.bioorg.2020.104399.

47 K. El-Adl, A. A. El-Helby, H. Sakr and A. Elwan, [1,2,4]Triazolo [4,3-a]quinoxaline and [1,2,4]triazolo[4,3-a]quinoxaline-1-thiol derived DNA intercalators: Design, synthesis, molecular docking, *in silico* ADMET profile and anti-proliferative evaluations, *New J. Chem.*, 2021, **45**, 881–897, DOI: 10.1039/D0NJ02990D.

48 C. A. Lipinski, F. Lombardo, B. W. Dominy and P. J. Feeney, *Adv. Drug Delivery Rev.*, 1997, **23**, 3, DOI: 10.1016/S0169-409X(96)00423-1.

49 D. E. V. Pires, T. L. Blundell and D. B. Ascher, pkCSM, *J. Med. Chem.*, 2015, **58**, 4066, DOI: 10.1021/acs.jmedchem.5b00104.

50 A. Beig, R. Agbaria and A. Dahan, *PLoS One*, 2013, **8**, e68237, DOI: 10.1371/journal.pone.0068237.

51 M. Zhang, G. Wang, X. Zhang, Y. Zheng, S. Lee, D. Wang and Y. Yang, Polyvinyl Alcohol/Chitosan and Polyvinyl Alcohol/Ag@MOF Bilayer Hydrogel for Tissue Engineering Applications, *Polymers*, 2021, **13**(18), 3151, DOI: 10.3390/polym13183151.

52 B. S. Alotaibi, A. K. Khan, Z. Kharaba, H. Yasin, R. Yasmin, M. Ijaz, M. Khan and G. Murtaza, Development of Poly(vinyl alcohol)-Chitosan Composite Nanofibers for Dual Drug Therapy of Wounds, *ACS Omega*, 2024, **9**(11), 12825–12834, DOI: 10.1021/acsomega.3c08856.